On the effect of morphology and particle-wall interaction on colloidal near-wall dynamics: Electronic supplementary information

1 Scattering amplitudes

1.1 Spherical particles

The scattering amplitude of a sphere with radius R and homogeneous scattering length distribution, $\rho(\mathbf{r}) = \rho$, under evanescent illumination is generally given by

$$B_{nw}(Q,\kappa,R) = \rho \int_0^{2\pi} d\phi \int_0^{\pi} d\theta \sin\theta \int_0^{R} dr\; r^2 \exp\left\{i\mathbf{Q}\cdot\mathbf{r}\right\} \exp\left\{-\frac{\kappa z}{2}\right\} \quad (1)$$

in polar coordinates. The scattering vector $\mathbf{Q}$ and the position vector $\mathbf{r}$ are given as

$$\mathbf{Q} = \begin{pmatrix} Q_{\parallel} \\ 0 \\ Q_{\perp} \end{pmatrix} \quad \text{and} \quad \mathbf{r} = \begin{pmatrix} \cos\phi\sin\theta\; r \\ \sin\phi\sin\theta\; r \\ \cos\theta\; r \end{pmatrix} \quad (2)$$

where we may select $Q_{\parallel} = Q_x$ because of the problems invariance with respect to rotation around the z-axis which is normal to the reflecting interface. With the substitutions $y = r/R$ and $\mu = \cos\theta$ we obtain

$$\begin{aligned} B_{nw}(Q,\kappa,R) \;=\; & R^3\rho \int_{-1}^{1} d\mu \\ & \int_0^1 dy\; y^2 \exp\left\{iQ_{\perp}Ry\mu\right\} \exp\left\{-\frac{\kappa Ry\mu}{2}\right\} \int_0^{2\pi} d\phi \exp\left\{iQ_{\parallel}Ry\cos\phi\sqrt{1-\mu^2}\right\} \end{aligned} \quad (3)$$

Using the tabulated integral

$$\int_0^{2\pi} d\alpha \exp\left\{iA\cos\alpha\right\} = 2\pi J_0(A) \quad (4)$$

with J_0 indicating the zeroth order Bessel function of the first kind we can write

$$B_{nw}(Q,\kappa,R) = 2\pi R^3\rho \int_{-1}^{1} d\mu \int_0^1 dy\; y^2 \exp\left\{iQ_\perp Ry\mu\right\} \exp\left\{-\frac{\kappa R y\mu}{2}\right\} J_0\left(Q_\parallel Ry\sqrt{1-\mu^2}\right). \tag{5}$$

Replacing the complex exponential by its trigonometric form we obtain

$$\begin{aligned} & B_{nw}(Q,\kappa,R) = 2\pi R^3\rho \left[\int_{-1}^{1} d\mu \right. \\ & \int_0^1 dy\; y^2 \cos\left(Q_\perp y\mu R\right) \exp\left\{-\frac{y\mu\kappa R}{2}\right\} J_0\left(Q_\parallel \sqrt{1-\mu^2} yR\right) \\ + \quad & i\int_0^1 dy\; y^2 \sin\left(Q_\perp y\mu R\right) \exp\left\{-\frac{y\mu\kappa R}{2}\right\} \left. J_0\left(Q_\parallel \sqrt{1-\mu^2} yR\right)\right]. \end{aligned} \tag{6}$$

1.2 Core-shell particles

Along the same line of argument, it is straightforward to derive the form amplitude for a spherical core-shell particle with scattering length densities ρ_C for $0 < r < R_C$ and ρ_S for $R_C < r < R$

$$\begin{aligned} & B_{nw}(Q_\parallel, Q_\perp, \kappa, R_C, R) = 2\pi R^3 \left(\int_{-1}^{1} d\mu \right. \\ & \rho_C \left[\int_0^\chi dy y^2 \cos(Q_\perp y\mu R) \exp\left\{-\frac{y\mu\kappa R}{2}\right\} J_0(Q_\parallel \sqrt{1-\mu^2} yR)\right. \\ + \quad & i\int_0^\chi dy y^2 \sin(Q_\perp y\mu R) \exp\left\{-\frac{y\mu\kappa R}{2}\right\} \left. J_0(Q_\parallel \sqrt{1-\mu^2} yR)\right] \\ + \quad & \rho_S \left[\int_\chi^1 dy y^2 \cos(Q_\perp y\mu R) \exp\left\{-\frac{y\mu\kappa R}{2}\right\} J_0(Q_\parallel \sqrt{1-\mu^2} yR)\right. \\ + \quad & i\int_\chi^1 dy y^2 \sin(Q_\perp y\mu R) \exp\left\{-\frac{y\mu\kappa R}{2}\right\} \left. \left. J_0(Q_\parallel \sqrt{1-\mu^2} yR)\right]\right) \end{aligned} \tag{7}$$

where $\chi = R_C/R$.

1.3 Spherical particles with surface roughness

An approximation for the form amplitude of spherical particles with small surface asperities can be derived, starting from the geometry shown in Fig.1. For the situation with a constant illumination profile the form amplitude may be separated into a part resulting from the spherical core body, B_C, and a

contribution from asperities which are very small compared to the reciprocal scattering vector with volume ΔV_j located at $\mathbf{r_j}$ on the surface of the core

$$B(Q,R) = \rho_C B_C + \sum_{j=1}^{N} \Delta V_j \rho_j \exp\left\{i\mathbf{Q}\cdot\mathbf{r_j}\right\}, \tag{8}$$

where ρ_j is the scatering length density of the j-th asperity.

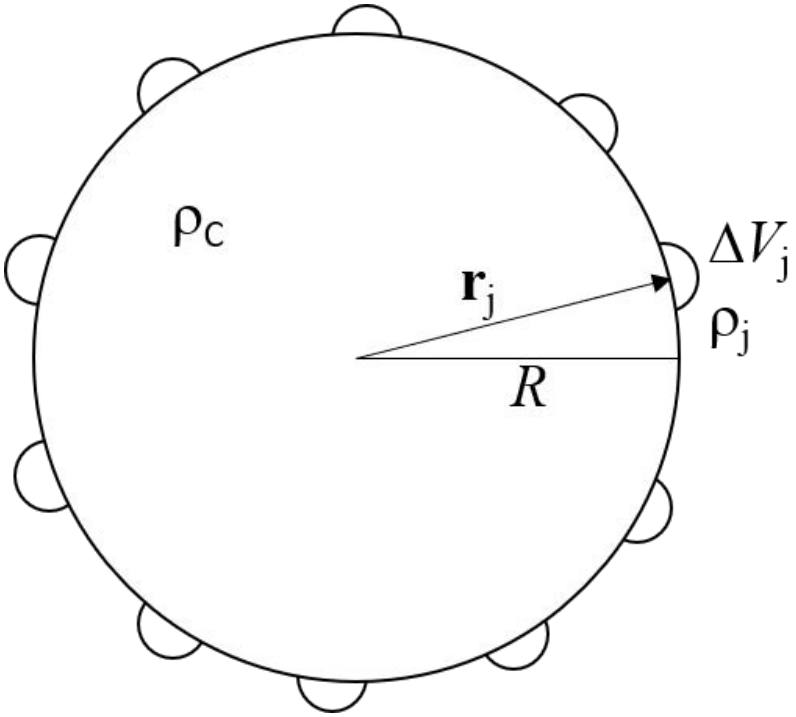

Figure 1: Schematic representation of a rough particle consisting of a spherical core with radius R and asperities of volume ΔV_j and scattering length density ρ_j located at $\mathbf{r}_j$.

Assuming that all asperities have the same scattering length density $\rho_j = \rho_a$ and writing the sum as a volume integral, we obtain

$$B(Q,R) = \rho_C B_C(Q,R) + \rho_a \int d\mathbf{r} \exp\left\{i\mathbf{Q}\cdot\mathbf{r}\right\}. \tag{9}$$

The volume integral can be turned into a surface integral assuming that the asperities are infinitely small and randomly distributed over the surface.

$$B(Q,R) \;=\; \rho_C B_C(Q,R) + \rho_a \Delta h R^2 \oint d\hat{\mathbf{s}} \exp\left\{i\mathbf{Q}\cdot\hat{\mathbf{r}}R\right\} \tag{10}$$

$$
\begin{aligned}
&= \rho_C B_C(Q,R) + \rho_a \Delta h R^2 \int_0^{2\pi}\int_{-1}^{1} d\mu \exp\{iQR\mu\} \\
&= \rho_C B_C(Q,R) + \rho_a \Delta h R^2 \frac{2\pi}{iQR}\left[\exp\{iQ\,R\} - \exp\{-iQR\}\right].
\end{aligned}
$$

Here, again we substituted $\cos\theta = \mu$ and the scattering vector was chosen to lie the z-direction, which is possible due to the spherical symmetry of the problem. Replacing the complex exponentials by their trigonometric representation, we obtain

$$
B(Q,R) = \rho_C B_C(Q,R) + \rho_a \Delta V \frac{\sin(QR)}{QR}. \tag{11}
$$

where the second term can be interpreted as the form amplitude of a thin shell with scattering length density ρ_a and an effective thickness Δh, which is small compared to the reciprocal scattering vector, corresponding to an effective volume $\Delta V = 4\pi R^2 \Delta h$.

For the situation in EWDLS, we have to include the exponentially decaying illumination profile into Eq.10 and consider the resulting symmetry break.

$$
\begin{aligned}
B_{nw}(Q,\kappa,R) &= \rho_C B_{C,nw}(Q,\kappa,R) + \rho_a \Delta h R^2 \oint d\hat{\mathbf{s}} \exp\{i\mathbf{Q}\cdot\hat{\mathbf{r}}R\} \exp\left\{-\frac{\kappa z}{2}\right\} \\
&= \rho_C B_{C,nw}(Q,\kappa,R) + \rho_a \Delta h R^2 \\
&\times \int_0^{2\pi}\int_{-1}^{1} d\mu \exp\left\{iR\left(Q_\parallel \cos\phi\sqrt{1-\mu^2} + Q_\perp \mu\right)\right\} \exp\left\{-\frac{\mu\kappa R}{2}\right\}
\end{aligned} \tag{12}
$$

After inverting the succession of integrations and applying again Eq. 4 the trigonometric representation of the form amplitude under evanescent illumination take the form

$$
\begin{aligned}
B_{nw}(Q,\kappa,R) &= \rho_C B_{C,nw}(Q,\kappa,R) + \rho_a \frac{\Delta V}{2} \\
&\times \left[\int_{-1}^{1} d\mu \cos(Q_\perp \mu R) \exp\left\{-\frac{\mu\kappa R}{2}\right\} J_0\left(Q_\parallel\sqrt{1-\mu^2}R\right)\right. \\
&+ \left. i\int_{-1}^{1} d\mu \sin(Q_\perp \mu R) \exp\left\{-\frac{\mu\kappa R}{2}\right\} J_0\left(Q_\parallel\sqrt{1-\mu^2}R\right)\right],
\end{aligned} \tag{13}
$$

which represents the limiting case of Eq. 7 for an infinitely thin shell.

2 Polydispersity effect on the dynamics of hard spheres

The effect of polydispersity on the near wall dynamics of non-interacting spherical particles is shown in Fig.2 for particles with Gaussian size distribution. Significant deviations from the monodisperse reference system are observed only for the largest standard deviations and the highest penetration depths of the evanescent wave. Intriguingly, the effect of polydispersity become larger with decreasing mean radius at constant standard deviation.

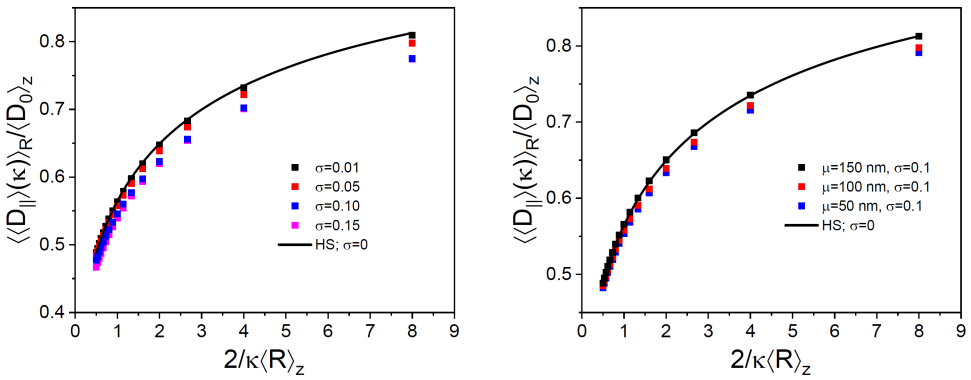

Figure 2: Normalized parallel diffusion coefficients versus normalized penetration depth for spherical particles with a Gaussian size distribution, interacting only by excluded volume. Left: mean radius $\mu = 100$ nm and relative standard deviations as indicated in the legend. Right: Relative standard deviation $\sigma = 0.1$ and mean radii as indicated in the legend. Symbols are data calculated as described in the main text and the full line represents the prediction for monodisperse hard sphere particles.

3 Original data and data analysis

Analysis of EWDLS intensity auto-correlation functions, $g_2(t)$ is notoriously hampered by a varying degree of homodyne-heterodyne mixing, as inhomogeneities of the reflecting surface and small impurities will inevitably lead to a static contribution to the scattering signal which leads to a reduction of the amplitude, A, of $g_2(t)$. Therefore, $g_2(t)$ has to be converted to the field correlation function $g_1(t)$ by solving the generalized Siegert relation [1]

$$g_2(t) = 1 + 2C_1 g_1(t) + (C_2 g_1(t))^2 \tag{14}$$

where $C_2 = 1 - \sqrt{1 - A}$ and $C_1 = C_2 - C_2^2$. In the following we show sets of correlation functions for the three particle types investigated, which illustrate the process of data analysis, the reproducibility of $g_2(t)$ and the data quality. All correlation functions were measured in the middle of the covered- $Q_\parallel^2$-range and at an angle of incidence $\alpha_i \approx 62.8$. The full set of data requires to validate this contribution will be made accessible on zenodo after publication

3.1 Data from SSi suspensions

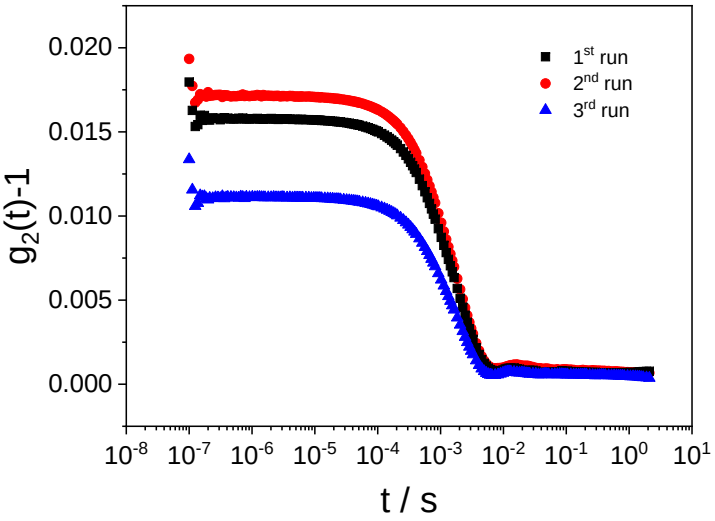

Figure 3: Time auto-correlation functions of the scattered intensity from the SSi suspension repeatedly measured as indicated in the legend at $Q_\parallel^2 = 24.67 \times 10^{-5}$ and $2/\kappa\langle R_H\rangle_z = 2.87$.

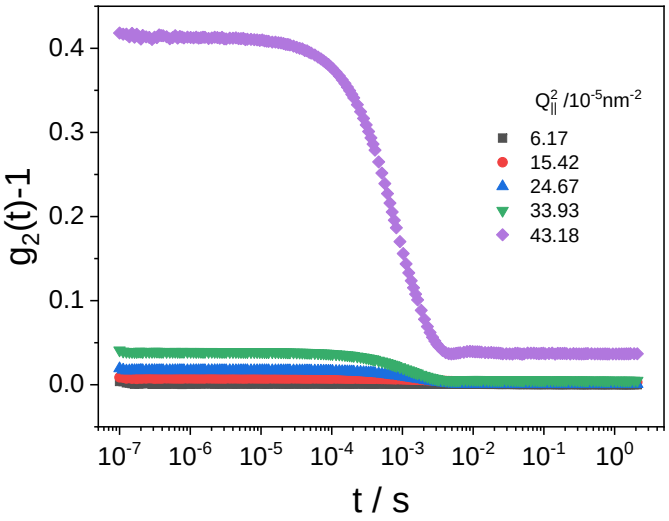

Figure 4: Time auto-correlation functions of the scattered intensity from an SSi suspension measured at $2/\kappa\langle R_H\rangle_z = 2.87$ and various at $Q_{\|}^2$ as indicated in the legend.

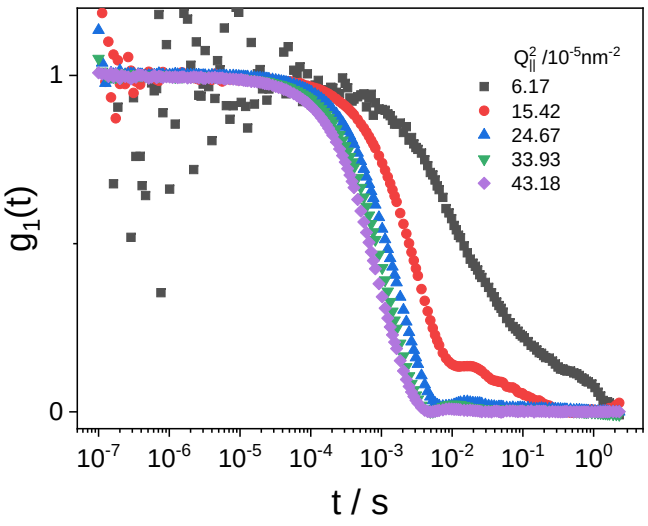

Figure 5: Time auto-correlations functions of the scattered field, $g_1(t)$, from an SSi suspension calculated from the $g_2(t)$-data shown in Fig.4 by solving the generalized Siegert relation of Eq.14. The original $g_2(t)$-data were measured at $2/\kappa\langle R_H\rangle_z = 2.87$ and various at $Q_{\|}^2$ as indicated in the legend.

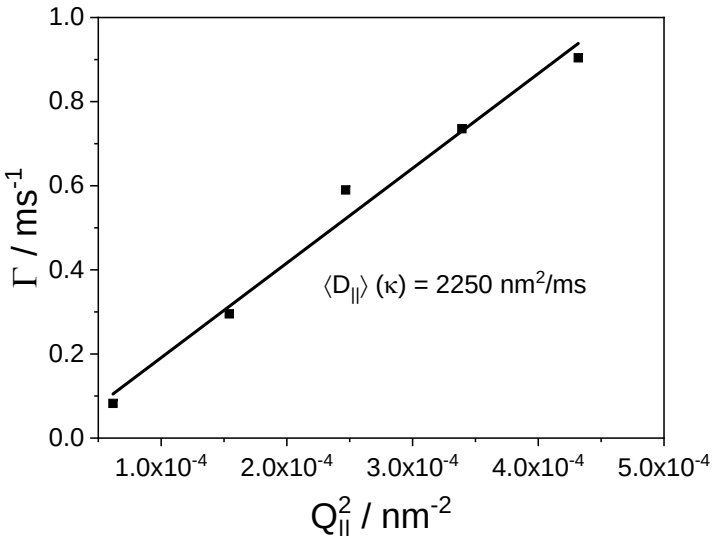

Figure 6: Initial slopes, Γ, of the $g_1(t)$-curves shown in Fig.5 plotted vs. $Q_\parallel^2$ (symbols). Not all measured correlation functions are shown. The full line represents a linear least squares fit resulting the averaged diffusion coefficient $\langle D_\parallel \rangle(\kappa) = 2250\mathrm{nm}^2/\mathrm{ms}$.

3.2 Data from HSi suspensions

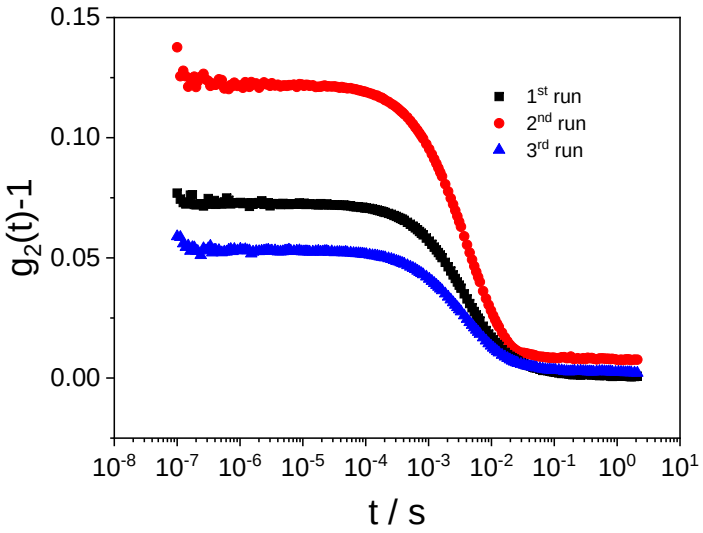

Figure 7: Time auto-correlation functions of the scattered intensity from an HSi suspension repeatedly measured as indicated in the legend at $Q_{\parallel}^2 = 26.33 \times 10^{-5}$ and $2/\kappa\langle R_H\rangle_z = 1.45$.

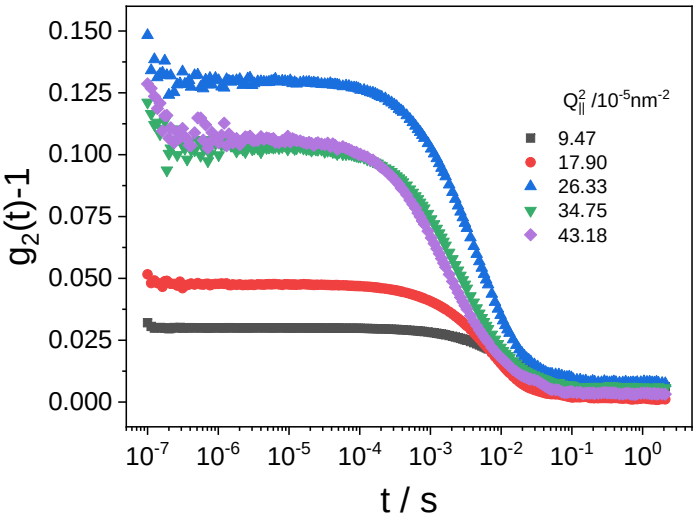

Figure 8: Time auto-correlation functions of the scattered intensity from an HSi suspension measured at $2/\kappa\langle R_H\rangle_z = 1.45$ and various at $Q_{\|}^2$ as indicated in the legend.

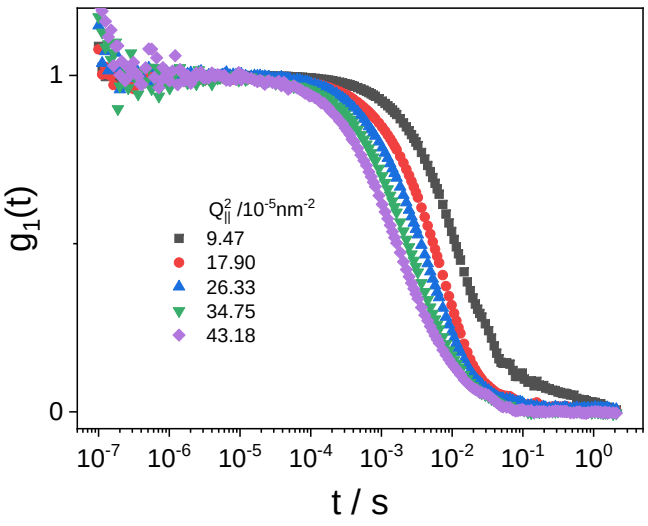

Figure 9: Time auto-correlation functions of the scattered field, $g_1(t)$, from an HSi suspension calculated from the $g_2(t)$-data shown in Fig.8 by solving the generalized Siegert relation of Eq.14. The original $g_2(t)$-data were measured at $2/\kappa\langle R_H\rangle_z = 1.45$ and various at $Q_{\|}^2$ as indicated in the legend.

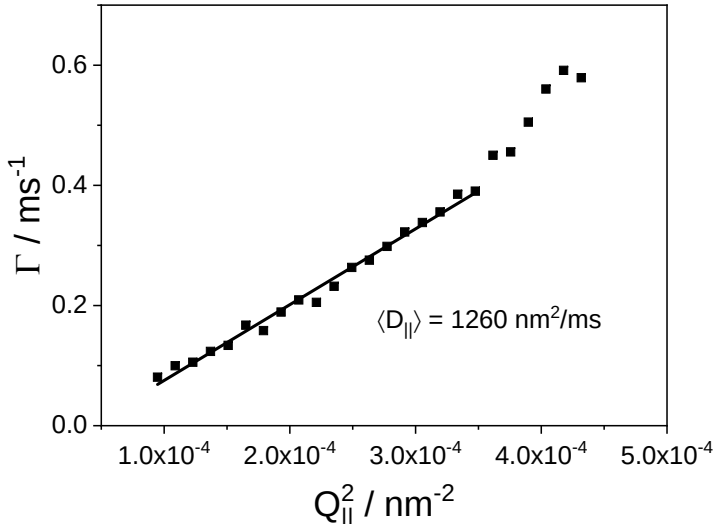

Figure 10: Initial slopes, Γ, of the $g_1(t)$-curves shown in Fig.9 plotted vs. $Q_\parallel^2$ (symbols). The full line represents a linear least squares fit resulting the averaged diffusion coefficient $\langle D_\parallel \rangle(\kappa) = 1260\mathrm{nm}^2/\mathrm{ms}$.

3.3 Data from RSi suspensions

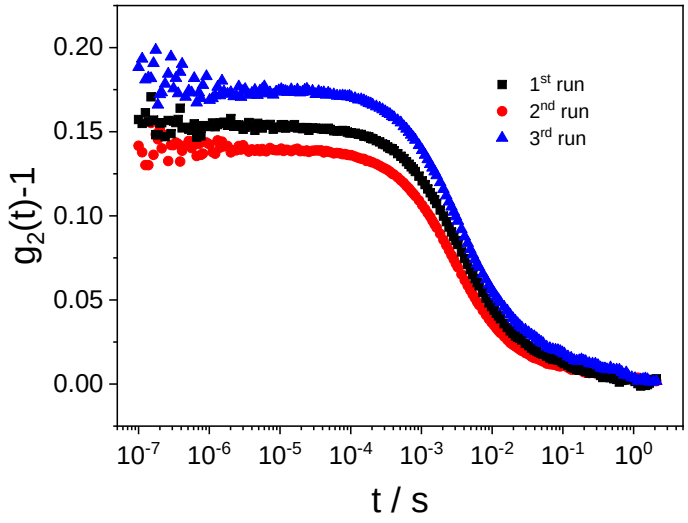

Figure 11: Time auto-correlation functions of the scattered intensity from an RSi suspension repeatedly measured as indicated in the legend at $Q_{\|}^2 = 23.7 \times 10^{-5}$ and $2/\kappa\langle R_H\rangle_z = 2.57$.

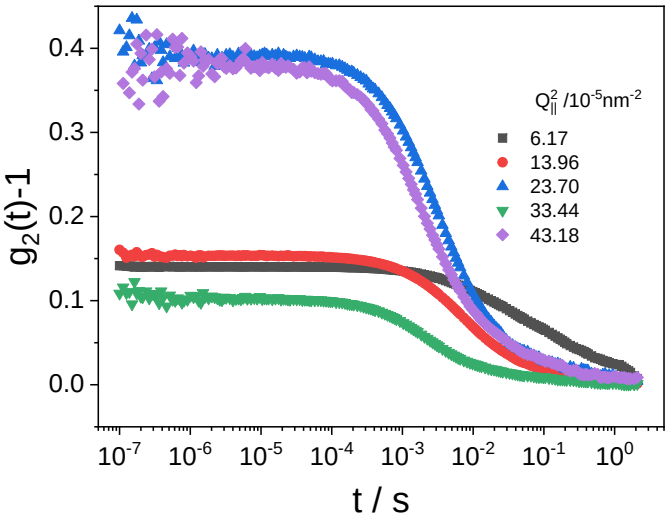

Figure 12: Time auto-correlation functions of the scattered intensity from an RSi suspension measured at $2/\kappa\langle R_H\rangle_z = 2.57$ and various at $Q_{\|}^2$ as indicated in the legend.

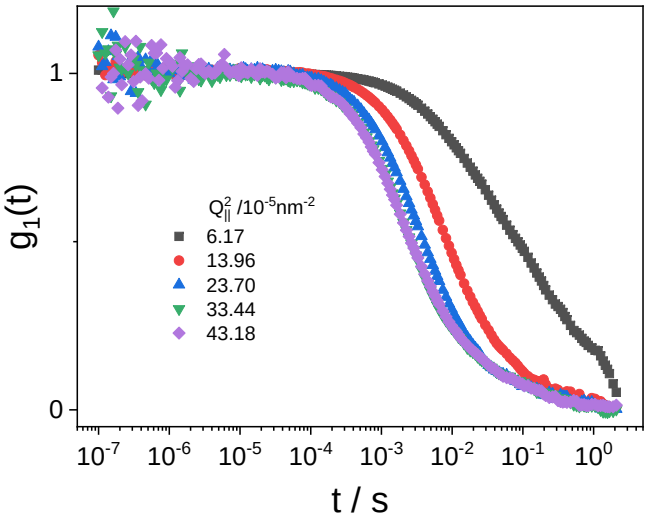

Figure 13: Time auto-correlation functions of the scattered field, $g_1(t)$, from an RSi suspension calculated from the $g_2(t)$-data shown in Fig.12 by solving the generalized Siegert relation of Eq.14. The original $g_2(t)$-data were measured at $2/\kappa\langle R_H\rangle_z = 2.57$ and various at $Q_{\|}^2$ as indicated in the legend.

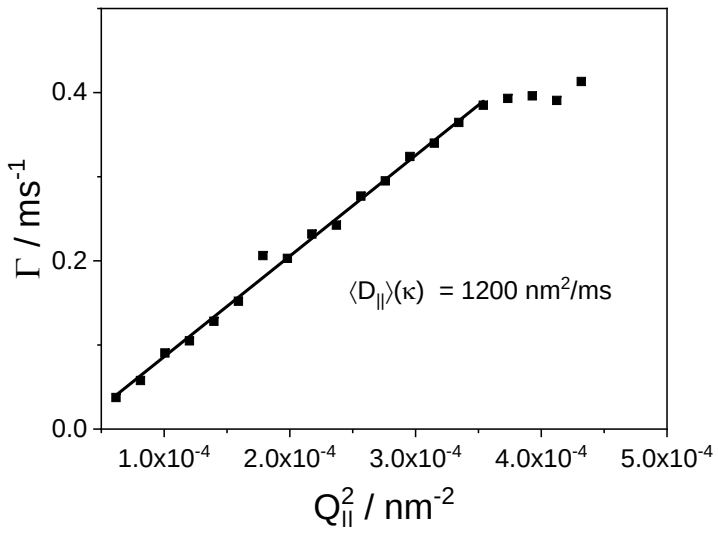

Figure 14: Initial slopes, Γ, of the $g_1(t)$-curves shown in Fig.13 plotted vs. $Q_\parallel^2$ (symbols). Not all measured correlation functions are shown. The full line represents a linear least squares fit resulting the averaged diffusion coefficient $\langle D_\parallel \rangle(\kappa) = 1200\mathrm{nm}^2/\mathrm{ms}$.

References

[1] Peter Holmqvist, Jan K. G. Dhont, and Peter R. Lang. Colloidal dynamics near a wall studied by evanescent wave light scattering: experimental and theoretical improvements and methodological limitations. *Journal of Chemical Physics*, 126(4):044707, 2007.